Improvement of Lithium-ion Battery Charging from The State-of-the-Art Industrial JEITA Guidelines to A Hybrid Temperature-Regulated Current Control

Hui-Wen Rebecca Liang, *Member, IEEE*, Yun Yang, *Member, IEEE*, and Shu Yuen Ron Hui, *Fellow, IEEE*

***Abstract*-This paper addresses some practical issues of the Japan Electronics and Information Technology Industries Association (JEITA) battery charging guidelines and common industrial practices. The issues involve the temperature-dependent charging profile that may not lead to optimal charging time. A hybrid temperature-regulated current control (HTRCC) is proposed and compared with common JEITA charging profile in order to minimize the charging time within the thermal limits of the battery. The form factor of the charging current is used for a quick verification that HTRCC can shorten the charging time. Based on an electro-thermal battery model, the minimum charging speed improvement rate (MCSI) compared to JEITA charging profile is also predicted. Practical measurements of the charging profile and charging time are included to confirm the theoretical analysis.**

***Keywords*-Hybrid temperature-regulated current control (HTRCC), Lithium-ion (Li-ion) battery, JEITA guidelines, electrical-thermal model, charging speed.**

I. INTRODUCTION

Overcharging lithium-ion (Li-ion) batteries at high temperature can be dangerous and could result in battery explosion or fire. According to [1], a one-in-200,000 breakdown of Lithium-ion batteries triggered a recall of almost six million Li-ion packs in 2006. In 2007, the Japan Electronics and Information Technology Industries Association (JEITA) and the Japan Battery Association published the JEITA battery charging guidelines [2] that have been widely adopted by electronics industries worldwide [3-5]. One important element in JEITA guidelines is the thermal limit of the battery. During the current-control (CC) charging mode, the charging current is set at different discrete levels based on the battery temperature in the entire charging process. As illustrated in Fig. 1, the charging current is less than the upper limit of the charge current when the temperature is relatively low within the temperature range between T_1 and T_2 (10°C) in order to avoid lithium deposit on the negative electrode. The normal charging temperature is within the range of T_2 and T_3 (45°C) when full charging current can be used. When the battery surface temperature increases to the range from T_3 to T_4, both reduced charging voltage and current have to be applied so as to avoid instability of the positive electrode crystal structure. T_4 is the maximum temperature limit above which no charging should occur.

Researches on battery charging considering the thermal factor have been recorded in [6-12]. References [6] and [7] focus on the ageing and degradation effects caused by the temperature on the Li-ion batteries. The thermal effects are incorporated into the battery modeling in [8-10]. Reference [11] compares the surface temperature of Li-ion cells based on different chemistries and capacities. A hybrid state-of-charge (SoC) and state-of-health (SoH) estimation technique for Li-ion battery based on surface temperature variation is reported in [12]. Those investigations are mainly focused on the internal characteristics of the Li-ion batteries, while the external features, such as the charging profiles, are not treated. Therefore, the industrial charging strategy in JEITA guidelines can be considered as the state-of-the-art technique with the temperature concern for Li-ion batteries.

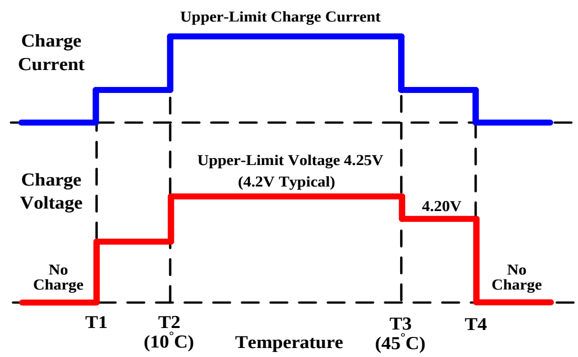

(a) JEITA guidelines for notebook applications

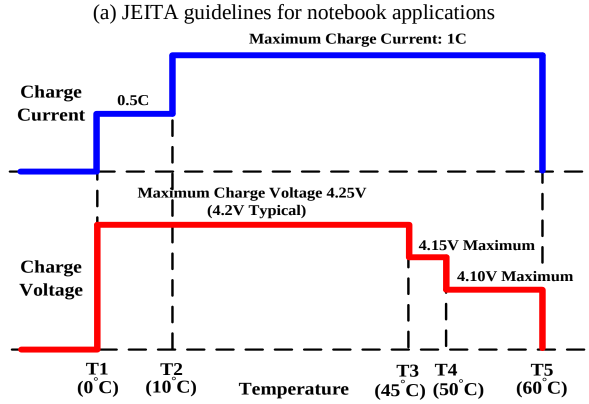

(b) JEITA guidelines for mobile phone applications

Fig. 1. Profiles of the JEITA charging guidelines [3] for charging Li-ion batteries in (a) notebook applications (b) single-cell handheld applications.

Paper received on XX, revised on XX and accepted on XX.
This project was partially supported by the NTU MediaTek Startup Fund 03INS001124C140. Rebecca Liang is with the Department of Electrical Engineering, Hong Kong Polytechnic University, Hung Hom, Hong Kong (email: rebecca.liang@polyu.edu.hk); Yun Yang is with the Department of Electrical Engineering, Hong Kong Polytechnic University, Hung Hom, Hong Kong (email: cacalotoyangyun@gmail.com). S.Y.R. Hui is with the School of Electrical and Electronic Engineering, Nanyang Technological University, Singapore 639798 (email: ron.hui@ntu.edu.sg) and also with Imperial College London, S. Kensington, London SW7 2AZ, U.K.

This paper aims to bridge the research gap by proposing a hybrid temperature-regulated current control (HTRCC), which evolves from the discrete temperature-regulated current control (DTRCC) in JEITA guidelines through a migration from a discrete temperature control to a continuous temperature control. Consequently, the form factor of the charging current of the proposed control is greater than that of the conventional control, leading to a faster charging speed and hence shorter charging time. The continuous temperature control of the HTRCC is established based on the electro-thermal model of a Li-ion battery under investigation. Electro-thermal modeling is not new because it has been used in light-emitting diode (LED) systems [13]. In this study, practical aspects such as accuracy and simplicity are considered for online implementations. An intuitive *RC*-based electrical model in [14] and the thermal model in [10] are coupled to form the electro-thermal battery model in this paper. The empirical results not only verify the analysis that the proposed control can improve the charging speed of Li-ion batteries as compared to the conventional control in JEITA guidelines, but also reveal that (i) the improvement is more significant when the ambient temperature is higher; (ii) a higher average charging current leads to a faster battery charging process; (iii) the total heat generation of the Li-ion in mainly determined by the root-mean-square (RMS) values of the charging current; and (iv) a larger form factor of the charging current signifies a faster charging speed of that method.

II. Practical Charging Issues Based on JEITA Guidelines

Recently, a series of charging tests on Li-ion batteries for commercial electronic products were conducted by an independent laboratory sponsored by the Hong Kong Consumer Council (HKCC). These tests were carried out with practical considerations such as charging time and battery temperature. Figs. 2(a) and (b) show two sets of measurements of the temperature-dependent charging profiles of the same electronic device under two different ambient temperatures of 22˚C and 35˚C. The charging profiles have two rated power levels, i.e., a normal-charging power level of 6W and a fast-charging power level of 12W. To ensure battery charging safety, the manufacturer of the tested product set 37˚C as the first upper-temperature limit of the battery surface temperature and 45˚C as the maximum temperature limit.

The test results at the ambient temperature of 22˚C (Fig. 2(a)) show that the fast charging cannot be sustained for a long time since the battery temperature will reach the upper limit quickly. The tested product is designed based on the JEITA guidelines to halve the charging power from 12W to 6W (by altering the charging current reference at the second stage of the constant power module while keeping the voltage reference at the first stage unchanged). Hence, the device is charged in the normal mode rather than the fast mode most of the time. As a result, it takes about 200 minutes for the estimated SoC to reach 100% and the battery temperature is well-regulated between 35˚C and 40˚C.

At the ambient temperature of 35˚C, the power charging profile is different, as can be seen from Fig. 2(b). Being compliant with the JEITA guidelines, the charging power is regulated to zero when the battery surface temperature stays close to the 45˚C limit during the period from 0 minute to 145 minutes. The SoC of the battery is changed from 0% to 78%. Therefore, the average charging power of the device in this case is even lower than the normal charging power of 6W, such that the total charging time is longer than the case in Fig. 2(a). Apparently, the SoC can only reach about 85% even after 240 minutes. The charging power is controlled to be pulsative after 145 minutes and the battery temperature oscillates between 37˚C and 42˚C.

The two JEITA-compliant charging profiles under the ambient temperatures of 22°C and 35°C highlight an important point that the ambient temperature can affect the total charging time of Li-ion batteries significantly. Specifically, (i) high ambient temperature reduces the temperature operating range and substantially increases the total charging time. Besides, (ii) the JEITA-compliant charging profiles are implemented using discrete charging current, which can lead to temperature ripples that in turn cause mechanical expansion and contraction in the battery pack.

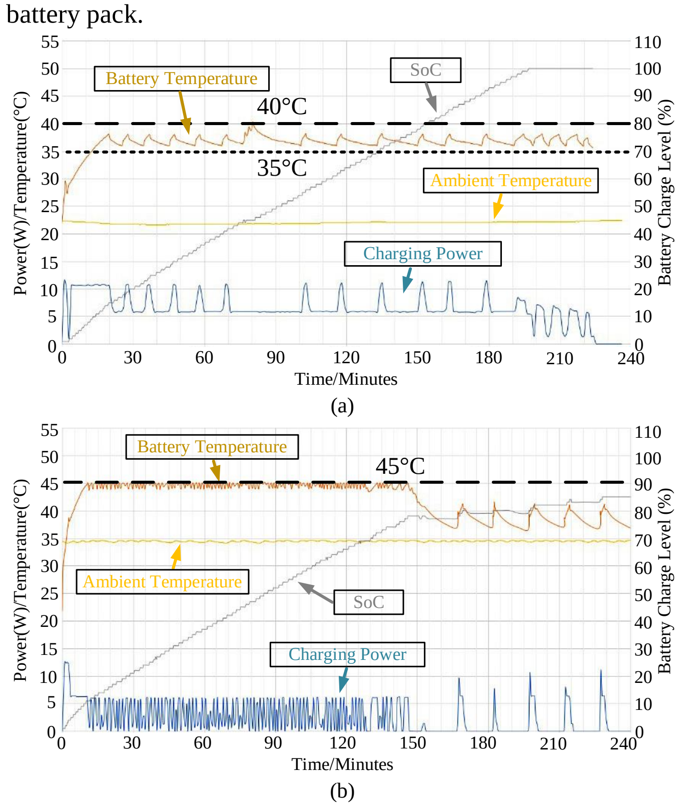

Fig. 2. Practical charging profile of a mobile device at an ambient temperature of (a) 22˚C and (b) 35˚C (Courtesy of HKCC).

III. Modeling of an Lithium-Ion Battery

In this paper, the Li-ion battery 3350mAh Panasonic NCR18650B, which has been widely adopted in the industry, is modeled for the HTRCC implementation. To achieve a good balance of accuracy and simplicity, the electrical and thermal characteristics of the Li-ion battery can be modeled by equivalent circuits, as shown in Fig. 3. The electrical model is simplified from the model in [14], which comprises an SoC-dependent open-circuit voltage source V_{oc}, an SoC-dependent internal series resistor R_{se}, and two SoC-dependent internal *RC* dynamic circuits with different time constants. Here, internal impedances are modeled based on the step response. The series resistor is modeled to emulate the instantaneous voltage drop, while the *RC* circuits are modeled to emulate both fast and slow dynamics (i.e., R_{trS} and C_{trS} for fast dynamics and R_{trL} and C_{trL} for slow dynamics). The SoC of the Li-ion battery is estimated based on the Coulomb-Counting method (CCM) as

$$\mathrm{SoC}(t) = \mathrm{SoC}(t_0) + \frac{\eta \int_{t_0}^{t} i_{\mathrm{B}}(t)dt}{C_{\mathrm{r}}} \tag{1}$$

where i_B is the instantaneous charging current, C_r is the rated capacity of the cell, η is the charging efficiency coefficient, and t_0 is the initial charging time.

The total internal resistance of the battery consists of the series resistance and the two resistances in the dynamic circuits, as

$$R_{\mathrm{B}}(\mathrm{SoC}) = R_{\mathrm{se}}(\mathrm{SoC}) + R_{\mathrm{trL}}(\mathrm{SoC}) + R_{\mathrm{trS}}(\mathrm{SoC}) \tag{2}$$

It is noted that R_B is a vital factor for the calculations of thermal dissipation. Moreover, R_{se}, R_{trL}, and R_{trs} are also temperature-dependent.

The thermal model is derived from the conventional models in [10] by using voltage and current to emulate the temperature and heat generation, respectively. Thus, the total heat generation of the battery (i.e., Q_{total}) can be modeled as a current source as shown in Fig. 3(b). The total heat generation comprises an irreversible heat generation (i.e., Q_{irr}) and a reversible heat generation (i.e., Q_{rev}) as

$$Q_{\mathrm{total}} = Q_{\mathrm{irr}} + Q_{\mathrm{rev}} \tag{3}$$

where the rates of Q_{irr} and Q_{rev} can be calculated based on the parameters of the electrical model in Fig. 3(a) as

$$\dot{Q}_{\mathrm{irr}} = [v_{\mathrm{B}} - V_{\mathrm{oc}}(\mathrm{SoC})]i_{\mathrm{B}} \tag{4}$$

$$\dot{Q}_{\mathrm{rev}} = i_{\mathrm{B}} T_{\mathrm{int}} \frac{\partial V_{\mathrm{oc}}(\mathrm{SoC})}{\partial T_{\mathrm{int}}} \tag{5}$$

where v_B of the terminal voltage of the battery and T_{int} is the internal battery temperature. The main contributor of irreversible heat generation is the mass transport loss. This irreversible term (4) is always positive. However, the reversible term (5) can be either positive or negative, which depends on the directions of i_B (i.e., i_B>0 for a battery in the charging mode). The internal battery temperature of the battery is determined by the total heat generation and heat exchange with the environment. The dynamics of the internal battery temperature can be expressed as

$$C_{\mathrm{p}} \frac{dT_{\mathrm{int}}}{dt} = \dot{Q}_{\mathrm{total}} - \dot{Q}_{\mathrm{exch}} \tag{6}$$

where C_p is the heat capacity. The dynamic equation in (6) can also be derived using Kirchhoff's circuit law based on the thermal model in Fig. 3(b).

Heat generated inside the battery is mainly transferred to the surface by means of conduction. Thus, the difference between the internal temperature (i.e., T_{int}) and surface temperature (i.e., T_{surf}) can be modeled simply as a voltage drop across an equivalent thermal resistor R_{is} even if the battery cells have layered structures with different thermal conductivities. The rate of heat exchange with the environment can be calculated based on

$$\dot{Q}_{\mathrm{exch}} = \frac{T_{\mathrm{int}} - T_{\mathrm{surf}}}{R_{\mathrm{is}}} \tag{7}$$

On the other hand, convection and radiation are the main channels of heat transfer from the battery surface to air. Therefore, its thermal resistance (i.e., R_{sa}) depends on the heat transfer coefficient (i.e., h_{out}) and surface area of the battery cell (i.e., A_{surf}) as

$$R_{\mathrm{sa}} = \frac{1}{h_{\mathrm{out}} A_{\mathrm{surf}}} \tag{8}$$

Then, the rate of heat exchange with environment can also be calculated based on

$$\dot{Q}_{\mathrm{exch}} = \frac{T_{\mathrm{surf}} - T_{\mathrm{amb}}}{R_{\mathrm{sa}}} \tag{9}$$

By substituting (8) into (9) to eliminate R_{sa},

$$\dot{Q}_{\mathrm{exch}} = h_{\mathrm{out}} A_{\mathrm{surf}} (T_{\mathrm{surf}} - T_{\mathrm{amb}}) \tag{10}$$

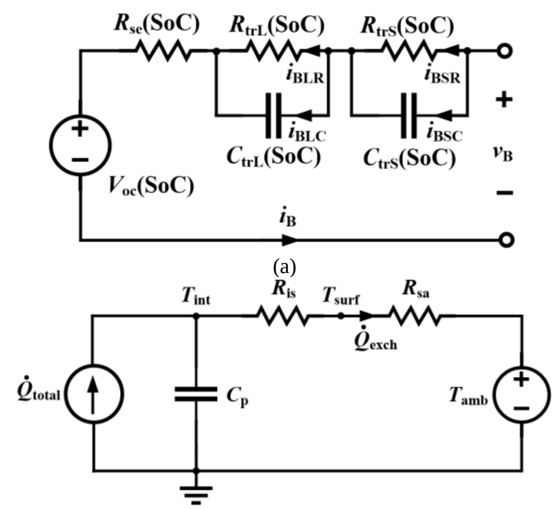

Fig. 3. (a) Electrical and (b) thermal models of the battery coupled with equations (3)-(5).

IV. Comparisons Between the Conventional Control in JEITA Guidelines and the Proposed Control

A. A Brief Review of the Conventional DTRCC in JEITA Guidelines

The DTRCC in JEITA guidelines is designed based on a physical fact that the Li-ion battery temperature is positively correlated to the charging current. Specifically, the Li-ion battery charged by a larger current can result in a higher temperature and vice versa. In practice, the surface temperature of the battery is commonly used for online monitoring and feedback control.

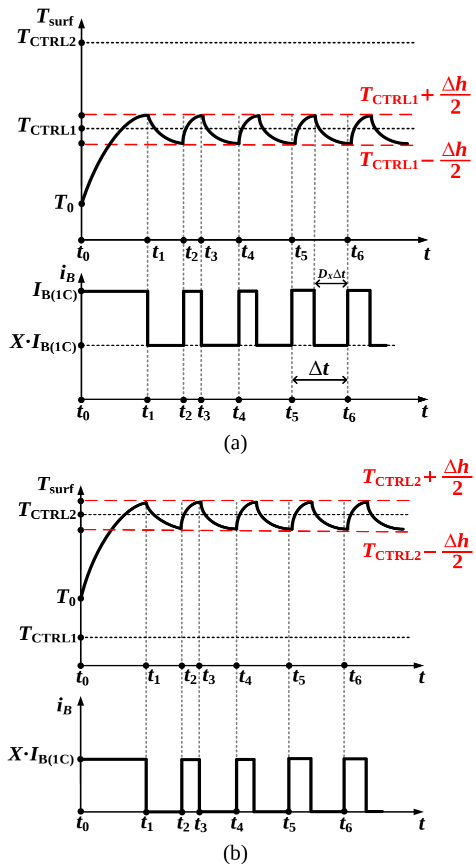

Fig. 4. Schematic diagrams of typical surface temperature and current profiles of a JEITA-compliant Li-ion battery with the reference (a) T_{CTRL1} and (b) T_{CTRL2}.

The schematic diagrams of typical surface temperature and current profiles of a JEITA-compliant Li-ion battery is depicted in Fig. 4. Two levels of temperature references (i.e., T_{CTRL1} and T_{CTRL2}) are illustrated in Fig. 4(a) and (b), respectively. By considering practical thermal inertia, hysteresis bands (i.e., $\frac{\Delta h}{2}$) are adopted for the two references. Thus, the current change is triggered by the surface temperature reaching the hysteresis boundaries rather than the references in practice. In Fig. 4(a), when the initial battery surface temperature is lower than the lower bound (i.e., $T_{\mathrm{surf}} < T_{\mathrm{CTRL1}} - \frac{\Delta h}{2}$), the charging current is controlled at $I_{\mathrm{B(1C)}}$ (i.e. 1C charging current of battery) based on the JEITA guidelines. As a result, the surface temperature is raised to the upper bound (i.e., $T_{\mathrm{CTRL1}} + \frac{\Delta h}{2}$) during the period from t_0 to t_1. Once the surface temperature reaches the upper bound, the charging current is reduced from $I_{\mathrm{B(1C)}}$ to $X{\cdot}I_{\mathrm{B(1C)}}$, where X is a coefficient between 0 and 1 (i.e., $0<X<1$). Since the charging current is significantly reduced, the corresponding battery temperature is reduced from the upper bound to the lower bound during the period from t_1 to t_2. When the battery temperature hits the lower bound, the charging current is resumed to be 1C. Thereupon, the same procedure repeats until the SoC of the battery meets the requirement. A similar charging scheme is also conducted for the reference T_{CTRL2}, as shown Fig. 4(b). T_{CTRL2} is close to the maximum temperature (i.e., T_{max}) (the battery temperature is prohibited from exceeding T_{max}). The charging current is controlled at $X{\cdot}I_{\mathrm{B(1C)}}$ when the battery surface temperature is equal to or lower than the lower bound (i.e., $T_{\mathrm{surf}} \le T_{\mathrm{CTRL2}} - \frac{\Delta h}{2}$). It is reduced to zero when the battery surface temperature is equal to or higher than the upper bound (i.e., $T_{\mathrm{surf}} \ge T_{\mathrm{CTRL2}} + \frac{\Delta h}{2}$). Within the hysteresis band, the charging current remains unchanged.

B. Control Algorithm of the Proposed HTRCC

The proposed HTRCC improves over the DTRCC of the JEITA guidelines by altering the explicit control law within the hysteresis band by a continuous temperature control law (i.e., charging current remains unchanged). The schematic diagrams of the surface temperature and current profile of the Li-ion battery controlled by the proposed HTRCC are plotted in Fig. 5. In both cases, the charging currents are controlled based on the JEITA guidelines during the initial period from t_0 to t_1 when the battery temperatures are lower than the lower bounds. Contrary to the conventional approach in Fig. 4, the HTRCC turns into the temperature control mode when the temperatures reach the references. After a short period of oscillations being caused by the thermal inertia and dynamic of the controllers, the battery temperatures can be well-regulated to track the references. The ideal charging currents are also constant at the steady state. However, by considering the variable electrical and thermal characteristics with different SoC and temperature values in practical scenarios, the charging currents will variate mildly, as shown in Fig. 5.

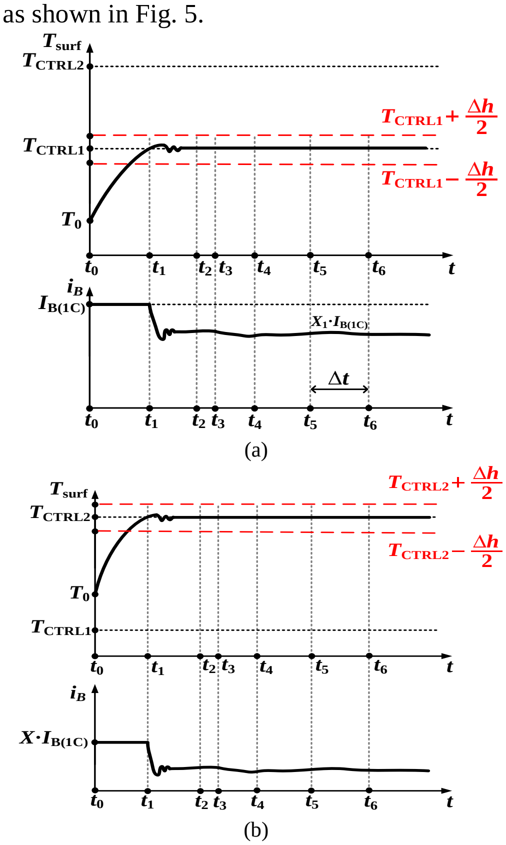

Fig. 5. Schematic diagrams of the Li-ion battery being controlled by the proposed control with the reference (a) T_{CTRL1} and (b) T_{CTRL2}.

The flowchart of the temperature control algorithm of the proposed HTRCC is shown in Fig. 6. Initially, the battery is charged with the discrete temperature control in JEITA guidelines. Then, battery surface temperature is compared to the reference. If the difference between the temperature reference and the battery temperature (i.e., $\Delta T = T_{\mathrm{CTRL}} - T_{\mathrm{surf}}$) is zero, which means the battery temperature reaches the reference, the continuous temperature control is activated. The continuous temperature control is implemented by a conventional proportional-integral (PI) control to provide charging current reference (i.e., I_{BREF}) based on ΔT in this paper. Simultaneously, the controller checks to see whether the battery temperature is within the hysteresis band (i.e., $|\Delta T| \leq \frac{\Delta h}{2}$). If $|\Delta T|$ deviates away from this range, the controller switches back to the conventional discrete temperature control in JEITA guidelines and ΔT is re-evaluated in the next iteration.

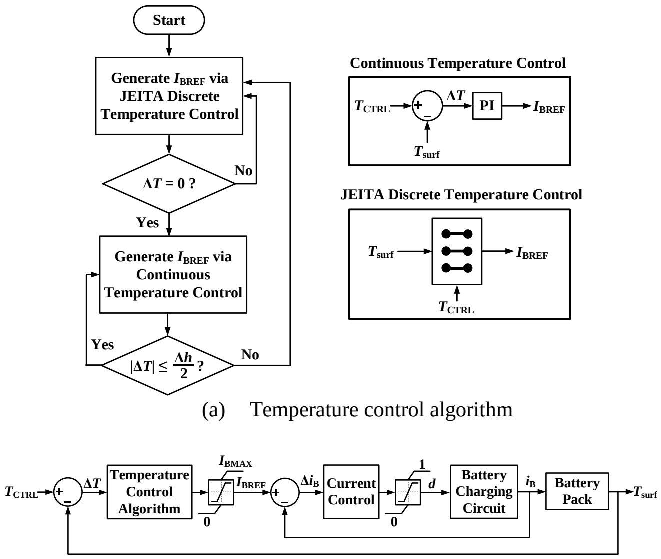

(a) Temperature control algorithm

(b) HTRCC

Fig. 6. Control algorithms of the proposed HTRCC.

The complete control block diagram of the proposed HTRCC is depicted in Fig. 6(b). It is a cascaded dual-loop control strategy that comprises the outer temperature control (as presented in Fig. 6(a)) and an inner current control. The outer temperature control provides charging current references for the inner current control, which further generate the duty ratios for the battery charging circuit. It is noted that the dynamics of the temperature control loop is slower than that of the inner current control loop, and the derived charging current references and duty ratios are bounded (i.e., $0 \leq I_{\mathrm{BREF}} \leq I_{\mathrm{BMAX}}$ and $0 \leq d \leq 1$). The inner current control is also implemented by a PI compensator in regulating the duty ratio of the switching signals for the battery charging circuit. The schematic diagram of the battery charging circuit is plotted as shown in Fig. 7(a). A series-series compensated inductive power transfer system, which can be considered as a controllable current source when the resonant frequencies of both transmitter and receiver are compensated at the switching frequency [15], is adopted for charging the battery load. Here, L_{p} and L_{s} are the self-inductances of the transmitter and receiver coils. C_{p} and C_{s} are the compensated capacitors. R_{p} and R_{s} are the equivalent-series-resistances (ESRs) of the transmitter and receiver resonators. M is the mutual inductance between the two coils. C_{f} is the output capacitor to filter the harmonics of the rectified current. S_1, S_2, S_3 and S_4 are the switching signals of the transmitter-side inverter. V_{dc} is the DC voltage source. v_{p} and v_{s} are the input and output voltages of the LC resonators. i_{p} and i_{s} are the transmitter and receiver currents. The sketchy waveforms of the switching signals and main electrical parameters are depicted, as shown in Fig. 7(b). Here, v_{p1} is the fundamental component of v_{p}. The amplitude of v_{p1} is proportional to the amplitude of i_{s}, which is in linear relationship to the battery charging current I_{B} [16]. Apparently, a larger duty ratio can result in a larger charging current. Therefore, for the inner current control loop, if the charging current is smaller than the current reference, Δi_{B} is positive. As a result, the output of the PI compensator (i.e., d) is increased, such that the charging current is increased accordingly. On the contrary, if the charging current is larger than the current reference, Δi_{B} is negative. Consequently, the charging current is decreased since d is reduced. For the outer loop, a larger charging current can result in a higher battery surface temperature (i.e., T_{surf}). Hence, if T_{surf} is lower than the temperature reference (i.e., T_{CTRL}), ΔT is positive. According to the temperature control algorithm in Fig. 6(a), for both continuous temperature control and JEITA discrete temperature control, a positive ΔT can lead to an increased current reference. Conversely, if T_{surf} is higher than T_{CTRL}, ΔT is negative, which leads to a decreased current reference.

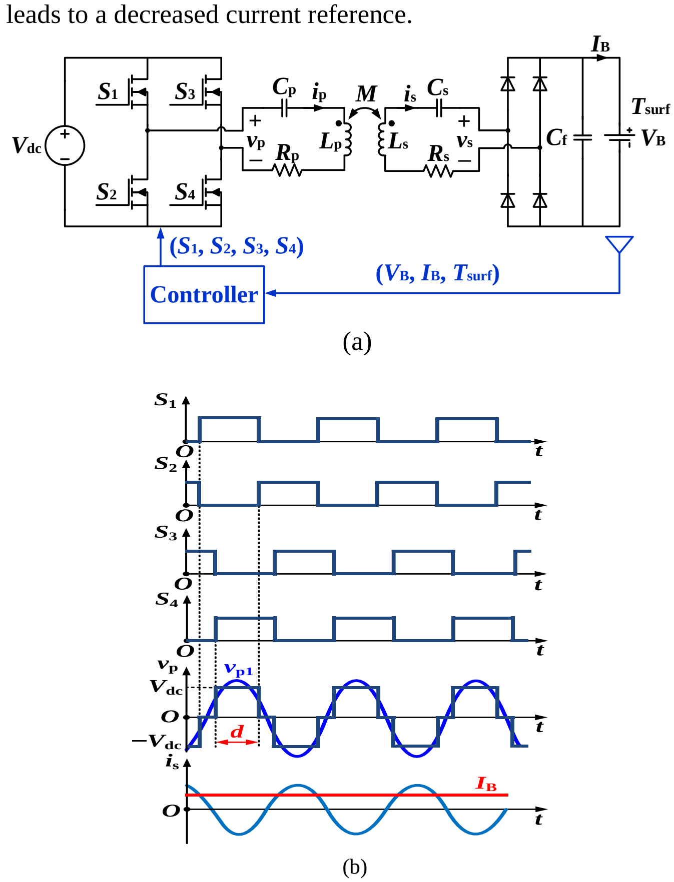

(a)

(b)

Fig. 7. Schematic diagrams of the (a) battery charging circuit and (b) switching signals and main electrical parameters.

C. Comparisons Between the Conventional Control and the Proposed Control

Based on the schematic diagrams in Figs. 4 and 5, the sketch maps of the charging current references versus different battery surface temperatures of the conventional control in JEITA guidelines and the proposed control is shown in Fig. 8. Note that the main difference between the two control methods is the control law selections within the hysteresis bands. Thus, the comparisons between the two control methods can be conducted based on this difference.

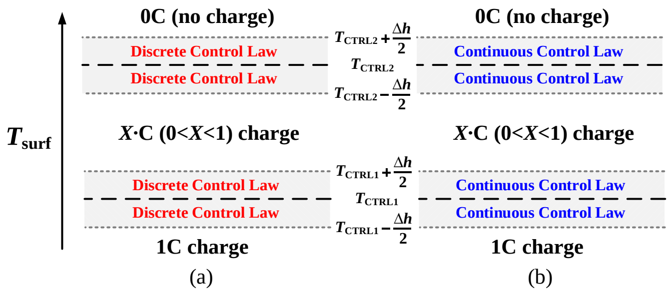

Fig. 8. Sketch maps of I_{BREF} versus T_{surf} for the (a) conventional control in JEITA guidelines and (b) proposed control.

By assuming the SoC of the batteries at t_5 in Figs. 4(a) and 5(a) are the same for both control methods, the respective electrical and thermal characteristics can be considered identical during the period from t_5 to t_6 without losing generality. Then, the rate of irreversible heat generation can be calculated based on the electrical-thermal model as

$$\dot{Q}_{\mathrm{irr}} = I_{\mathrm{B(rms)}}^2 R_{\mathrm{se}} + I_{\mathrm{BLR(rms)}}^2 R_{\mathrm{trL}} + I_{\mathrm{BSR(rms)}}^2 R_{\mathrm{trS}} \tag{11}$$

where $I_{\mathrm{B(rms)}}$, $I_{\mathrm{BLR(rms)}}$, and $I_{\mathrm{BSR(rms)}}$ are the root-mean-square (RMS) values of i_{B}, i_{BLR}, and i_{BSR} in Fig. 3(a). It is well-known that the RMS value of an AC signal must be greater than the average value of that signal, while the RMS value of a DC signal equals to the average value of that signal. Therefore, by considering the extreme cases of the dynamic capacitors in the electrical model (i.e., C_{trL} and C_{trS}), $I_{\mathrm{BLR(rms)}}$ and $I_{\mathrm{BSR(rms)}}$ must satisfy the following inequations as

$$I_{\mathrm{B(avg)}} \le I_{\mathrm{BLR(rms)}} \le I_{\mathrm{B(rms)}} \tag{12.1}$$
$$I_{\mathrm{B(avg)}} \le I_{\mathrm{BSR(rms)}} \le I_{\mathrm{B(rms)}} \tag{12.2}$$

where $I_{\mathrm{B(avg)}}$ is the average value of i_{B}.

By substituting (12) into (11) to eliminate $I_{\mathrm{BLR(rms)}}$ and $I_{\mathrm{BSR(rms)}}$, the minimum and maximum rate of irreversible heat generation of the battery can be derived as

$$\dot{Q}_{\mathrm{irr(min)}} = I_{\mathrm{B(rms)}}^2 R_{\mathrm{se}} + I_{\mathrm{B(avg)}}^2 (R_{\mathrm{trL}} + R_{\mathrm{trS}}) \tag{13.1}$$
$$\dot{Q}_{\mathrm{irr(max)}} = I_{\mathrm{B(rms)}}^2 R_{\mathrm{B}} \tag{13.2}$$

Besides, the rate of reversible heat generation of the battery during the period from t_5 to t_6 can be calculated based on (5) as

$$\dot{Q}_{\mathrm{rev}} = I_{\mathrm{B(avg)}} T_{\mathrm{int}} \frac{\partial V_{\mathrm{oc}}(\mathrm{SoC})}{\partial T_{\mathrm{int}}} \tag{14}$$

Considering (14) with (13.1) and (13.2), respectively, yield the minimum and maximum rates of the total heat generation as

$$\dot{Q}_{\mathrm{total(min)}} = A_1 I_{\mathrm{B(avg)}}^2 + B_1 I_{\mathrm{B(avg)}} \tag{15.1}$$
$$\dot{Q}_{\mathrm{total(max)}} = A_2 I_{\mathrm{B(avg)}}^2 + B_1 I_{\mathrm{B(avg)}} \tag{15.2}$$

where

$$A_1 = k_{\mathrm{f}}^2 R_{\mathrm{se}} + R_{\mathrm{trL}} + R_{\mathrm{trS}} \tag{15.3}$$
$$A_2 = k_{\mathrm{f}}^2 R_{\mathrm{B}} \tag{15.4}$$
$$B_1 = T_{\mathrm{int}} \frac{\partial V_{\mathrm{oc}}(\mathrm{SoC})}{\partial T_{\mathrm{int}}} \tag{15.5}$$

and k_{f} is the form factor (i.e., $k_{\mathrm{f}} = \frac{I_{\mathrm{B(rms)}}}{I_{\mathrm{B(avg)}}} \ge 1$).

For the conventional control, the average and RMS values of the charging current during the period from t_5 to t_6 are:

$$I_{\mathrm{B(avg)}}(\mathrm{JEITA}) = I_{\mathrm{B(1C)}}(1 - D_x + X \cdot D_x) \tag{16}$$
$$I_{\mathrm{B(rms)}}(\mathrm{JEITA}) = I_{\mathrm{B(1C)}}\sqrt{1 - D_x + X^2 \cdot D_x} \tag{17}$$

where D_{x} is defined in Fig. 4(a). Hence, the form factor of the waveform for the conventional control can be further derived as

$$k_{\mathrm{f}}(\mathrm{JEITA}) = \frac{I_{\mathrm{B(1C)}}}{I_{\mathrm{B(avg)}}(\mathrm{JEITA})}\sqrt{\frac{I_{\mathrm{B(avg)}}(\mathrm{JEITA})}{I_{\mathrm{B(1C)}}}(1+X) - X} > 1 \tag{18}$$

For the proposed HTRCC control, due to the variations are negligible during this short period, the average and RMS values are equal. That is,

$$I_{\mathrm{B(avg)}}(\mathrm{new}) = I_{\mathrm{B(rms)}}(\mathrm{new}) = X_1 \cdot I_{\mathrm{B(1C)}} \tag{19}$$

where X_1 is a coefficient between X and 1 (i.e., $X<X_1<1$). Thus, the form factor of the waveform is unity for the proposed control as

$$k_{\mathrm{f}}(\mathrm{new}) = 1 \tag{20}$$

By substituting (20) into (15.3) and (15.4), it is easy to derive that the coefficients A_1 and A_2 are identical for the proposed control such that the minimum and maximum rates of the total heat generation are equal.

$$\dot{Q}_{\mathrm{total}}(\mathrm{new}) = R_{\mathrm{B}} I_{\mathrm{B(avg)}}^2(\mathrm{new}) + B_1 I_{\mathrm{B(avg)}}(\mathrm{new}) \tag{21}$$

The charging speed of the two methods can be compared via the average charging currents of the batteries with the same heat generation. Specifically, under the premise that the total heat generation of the conventional control and proposed control are equal (i.e., $\dot{Q}_{\mathrm{total}}(\mathrm{JEITA}) = \dot{Q}_{\mathrm{total}}(\mathrm{new})$), the control method with a larger average charging current can indicate that the charging speed of this method is faster.

To simplify the analysis, the ratio between $I_{\mathrm{B(avg)}}(\mathrm{new})$ and $I_{\mathrm{B(avg)}}(\mathrm{JEITA})$, i.e., $\mathrm{CSI} = \frac{I_{\mathrm{B(avg)}}(\mathrm{new})}{I_{\mathrm{B(avg)}}(\mathrm{JEITA})}$, is defined as the charging speed improvement rate. If the minimum charging speed improvement rate (*MCSI*) is greater than one (i.e., *MCSI*>1), the proposed control can enhance the performance by reducing the charging time, as compared to the conventional control in JEITA guideline.

According to the analysis in Appendix-*A*, $I_{\mathrm{B(avg)(min)}}(\mathrm{JEITA})$, which is the average charging current corresponding to $\dot{Q}_{\mathrm{total(min)}}(\mathrm{JEITA})$, is greater than $I_{\mathrm{B(avg)(max)}}(JEITA)$, which corresponds to $\dot{Q}_{\mathrm{total(max)}}(\mathrm{JEITA})$. Therefore, the characteristics of *MCSI* is analyzed based on

$$\dot{Q}_{\mathrm{total(min)}}(\mathrm{JEITA}) = \dot{Q}_{\mathrm{total}}(\mathrm{new}) \tag{22}$$

By substituting (15.1) and (21) into (22) yields

$$\begin{aligned} A_1 I^2_{\mathrm{B(avg)(min)}}(\mathrm{JEITA}) + B_1 I_{\mathrm{B(avg)(min)}}(\mathrm{JEITA}) \\ = R_{\mathrm{B}} I^2_{\mathrm{B(avg)}}(\mathrm{new}) + B_1 I_{\mathrm{B(avg)}}(\mathrm{new}) \end{aligned} \tag{23}$$

By substituting (18), (19) and (A2) into (23) to eliminate $I_{\mathrm{B(avg)(min)}}(\mathrm{JEITA})$, $I_{\mathrm{B(avg)}}(\mathrm{new})$, and k_{f} yields

$$MCSI_{(h)} = \frac{\left[W_{(h)} + \sqrt{W_{(h)}^2 + 4pR_{\mathrm{B}} I_{\mathrm{B(1C)}} f_{(h)}(X_1)}\right] X_1}{2 f_{(h)}(X_1)} \tag{24}$$

where $p = \frac{R_{\mathrm{trL}} + R_{\mathrm{trS}}}{R_{\mathrm{B}}}$, $m = \frac{B_1}{R_{\mathrm{B}}}$, $W_{(\mathrm{h})} = (1-p)(1+X)R_{\mathrm{B}} I_{\mathrm{B(1C)}} + mR_{\mathrm{B}}$, and $f_{(\mathrm{h})}(X_1) = R_{\mathrm{B}} I_{\mathrm{B(1C)}} X_1^2 + mR_{\mathrm{B}} X_1 + R_{\mathrm{B}} I_{\mathrm{B(1C)}}(1-p)X$. The subscript "h" refers to the case where X_1 is higher than X ($X<X_1<1$). According to the proof in Appendix-*B*, the *MCSI* must be greater than one.

Similar derivation of *MCSI* for the cases in Figs. 4(b) and 5(b) (case where $0<X_1<X$) can also be made as

$$MCSI_{(l)} = \frac{W_{(l)} + \sqrt{W_{(l)}^2 + 4pR_{\mathrm{B}} I_{\mathrm{B(1C)}} X_1 f_{(l)}(X_1)}}{2 f_{(l)}(X_1)} \tag{25}$$

where $W_{(l)} = (1-p)XR_{\mathrm{B}} I_{\mathrm{B(1C)}} + mR_{\mathrm{B}}$ and $f_{(l)}(X_1) = R_{\mathrm{B}} I_{\mathrm{B(1C)}} X_1 + mR_{\mathrm{B}}$. The subscript "*l*" refers to the case where X_1 is lower than X. Obviously, this *MCSI* is also greater than one. Hence, the charging speed of the proposed control is faster than that of the conventional control in the JEITA guidelines.

Simulations are carried out using Matlab to plot the curves of the *MCSI* versus X_1 with the major parameters given in Table I. According to the specifications of the battery, the 1C battery charging current (i.e., $I_{\mathrm{B(1C)}}$) is 3.35 A. The coefficient X is set to be 0.5 based on the practical routine. The internal battery temperature is assumed to be 45˚C (318.15 K). The parameters p, R_{B}, and $\frac{\partial V_{\mathrm{oc}}(\mathrm{SoC})}{\partial T_{\mathrm{int}}}$ of B_1 are determined based on the practical measurements (as provided in Appendix-*C*). As the factor p mostly lies in between 0.25 and 0.45 for the battery at different SoC, two cases (i.e., p_1=0.25 and p_2=0.45) are studied, respectively. The parameter m is constantly changing during the charging process since the parameters B_1 and R_{B} are not fixed values and can be affected by the temperature. m ranges from -2 (i.e., $\frac{B_{1(\min)}}{R_{\mathrm{B}(\min)}} \approx -2$; $B_{1(\min)}$ is negative) to 1 (i.e., $\frac{B_{1(\max)}}{R_{\mathrm{B}(\min)}} \approx 1$; $B_{1(\max)}$ is positive), and is greater than 0 under most SoCs during charge. Based on (23) and (24), the curves of MCSI versus X_1 with p=0.25 and p=0.45 are plotted in Fig. 9. Note that the MCSIs are greater than one for all the cases, indicating that the proposed control can be faster than the conventional JEITA-compliant control. Besides, since the parameters m can significantly affect the MCSI, the coefficient X_1 needs a case-by-case design. The optimal X_1 can be obtained by solving the partial derivatives of *MCSI* with respect to X_1 (i.e., $\frac{\partial MCSI}{\partial X_1}$) when the parameters p and m are determined. By comparing the results in Figs. 9(a),(b) and Figs. 9(c),(d), the *MCSI* for a lower current case (i.e., $0<X_1<X$) is more significant than that for a higher current case (i.e., $X<X_1<1$). This corresponds to the fact that a higher ambient temperature condition for the battery charging leaves only a small temperature increase margin.

TABLE I. MAIN PARAMETERS ADOPTED IN SIMULATION

Descriptions	Value
1C charging current (i.e., $I_{\mathrm{B(1C)}}$)	3.35 A
Coefficient X	0.5
Internal battery temperature T_{int}	318 K
Factor p_1	0.25
Factor p_2	0.45

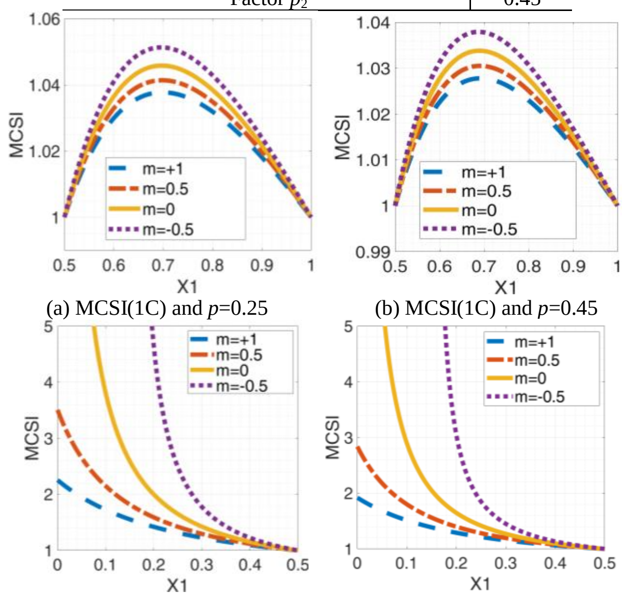

(a) MCSI(1C) and p=0.25 (b) MCSI(1C) and p=0.45

(c) MCSI(XC) and p=0.25 (d) MCSI(XC) and p=0.45

Fig. 9. The curves of MCSI versus X_1.

V. EXPERIMENTAL VERIFICATIONS

Experiments are conducted on the setup as shown in Fig. 10. The Li-ion battery 3350mAh Panasonic NCR18650B is placed inside the thermal incubator Binder KB53 for charging control. The thermal incubator is manually tuned to keep the ambient temperature at 32.4˚C, 34.1˚C, 44.2˚C, and 44.6˚C for the battery charging processes. The battery surface temperature is measured using a *K*-type thermocouple and fed back into the digital controller, which is implemented using the Texas Instrument's digital signal processor (DSP) TMS320F28335, to regulate the battery charging circuit. In the digital controller, the two temperature references (i.e., T_{CTRL1} and T_{CTRL2}) and the hysteresis band (i.e., Δh) are set to be 37.3˚C, 45˚C, and 0.7˚C, respectively. Both the outer continuous temperature control and inner current control of the proposed HTRCC are implemented by the conventional PI control with the parameters of $K_{P(out)}$=2.2, $K_{I(out)}$=0.002, $K_{P(in)}$=3, and $K_{I(in)}$=2000. The ambient temperature, battery surface temperature, battery charging current, and the battery terminal voltage (i.e., T_{amb}, T_{surf}, i_B, and v_B) are measured by the Agilent 34970A Data Logger with 34901A Multiplexer at a recording rate of 1/s. All the experiments are conducted on the batteries being rest for at least 1.5-hour after the full discharge. Thus, the initial SoC of the batteries is set as 0% for comparison purpose. The practical implementation of the battery charging circuit is depicted in Fig. 11. Two GaN half-bridge power stages LMG5200 are adopted for the transmitter inverter. The self-inductances of the transmitter and receiver coils are 48.38 μH and 48.38 μH, respectively. The mutual inductance between the two coils is 8.52 μH. The compensated capacitances are 52.3 nF and 52.2 nF, respectively. The ESRs of the two resonators are 0.13 Ω and 0.13 Ω. The Schottky diode IN5822 with a forward voltage of 0.53 V is adopted for the passive rectifier. The filter capacitor is 100 μF. A 0.1 Ω high-current-low-resistance resistor OMCTGHLV-R100JE167916 is connected in series with the battery load for charging current sensing. A precision isolation amplifier AMC1100 is adopted to adapt the voltage requirement of the analogue-to-digital (ADC) input of the DSP. The output of the K-type thermocouple is also amplified by an amplifier OPA350 to meet such a requirement.

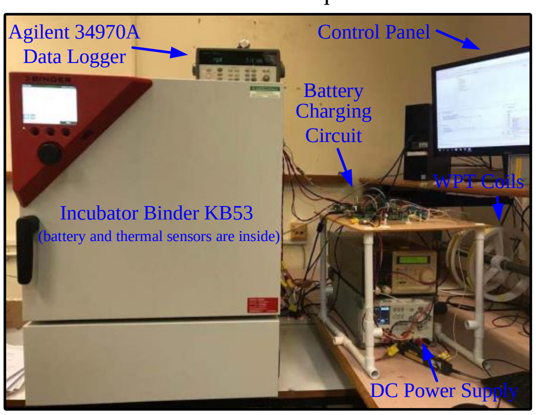

Fig. 10. A photograph of the setup.

Fig. 12 shows the waveforms of the measured temperatures, charging currents, and estimated SoC of the batteries under T_{amb}=34.1˚C for both control methods. The ambient temperatures are well-regulated by the thermal incubator. Since the ambient temperature is below 37.3˚C, the charging current of the conventional control follows the JEITA guidelines to track the alternative references of 1C (i.e., 3.35 A) and 0.5C (i.e., 1.675A). Accordingly, the battery surface temperature fluctuates within the hysteresis band from 36.95˚C and 37.65˚C. The SoC of the battery being charged by the conventional control is estimated and plotted in Fig. 12(c). The conventional control needs 68.08 minutes for the battery to reach the SoC of 70%. The charging current of the proposed control is between 1C (i.e., 3.35 A) and 0.5C (i.e., 1.675A), as shown in Fig. 12(b). The corresponding battery surface temperature slightly variates between 37˚C and 37.3˚C within the hysteresis band at steady state. The SoC of the battery being regulated by the proposed control is also estimated and plotted in Fig. 12(c). The proposed control only requires 64.07 minutes for the battery to reach the SoC of 70%. Compared to the conventional control, the charging speed is improved by about 5.9%.

The waveforms of the measured temperatures, charging currents, and SoC (estimated from the measured charging current according to CCM in equation (1)) of the batteries under T_{amb}=44.2˚C for both control methods are shown in Fig. 13. The ambient temperatures are also well-regulated by the thermal incubator. In this case, the ambient temperature is above 44.2˚C. Hence, the charging current of the conventional control is changed between 0.5C (i.e., 1.675 A) and 0. The corresponding battery surface temperature fluctuates within the hysteresis band from 44.65˚C and 45.35˚C. The battery with the conventional control takes about 158.94 minutes to reach the SoC of 70%, as can be seen from the results in Fig. 13(c). The charging current of the proposed control is between 0.5C (i.e., 1.675 A) and 0, as shown in Fig. 13(b). The corresponding battery surface temperature slightly variates between 44.9˚C and 45.2˚C within the hysteresis band. The battery with the proposed control takes only about 131.1 minutes to reach the SoC of 70%, which means that the charging speed of the proposed control is enhanced by about 17.52% as compared to that of the conventional control.

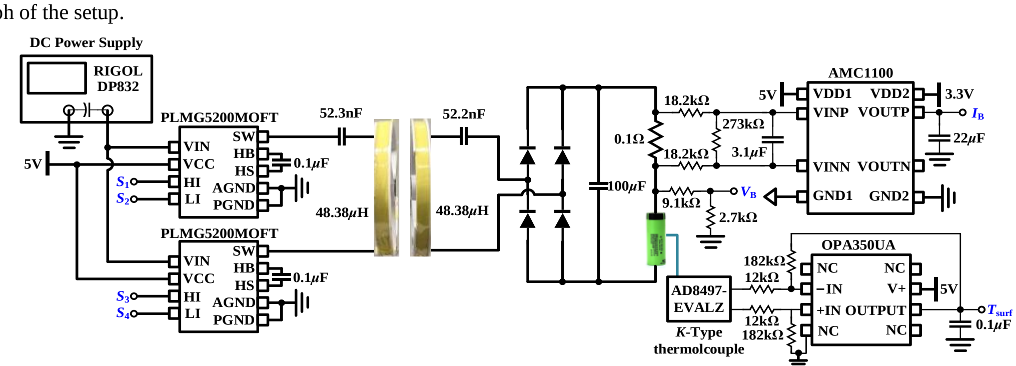

Fig. 11. Practical Implementation of the battery charging circuit.

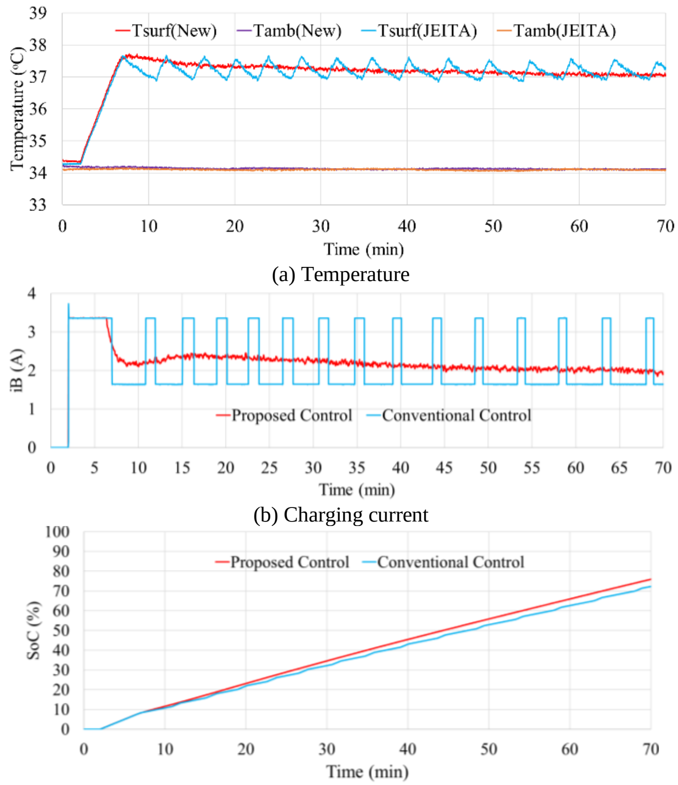

(a) Temperature

(b) Charging current

(c) SoC

Fig. 12. Measured temperatures, charging currents, and SoC of the batteries under the ambient temperature of 34.1˚C.

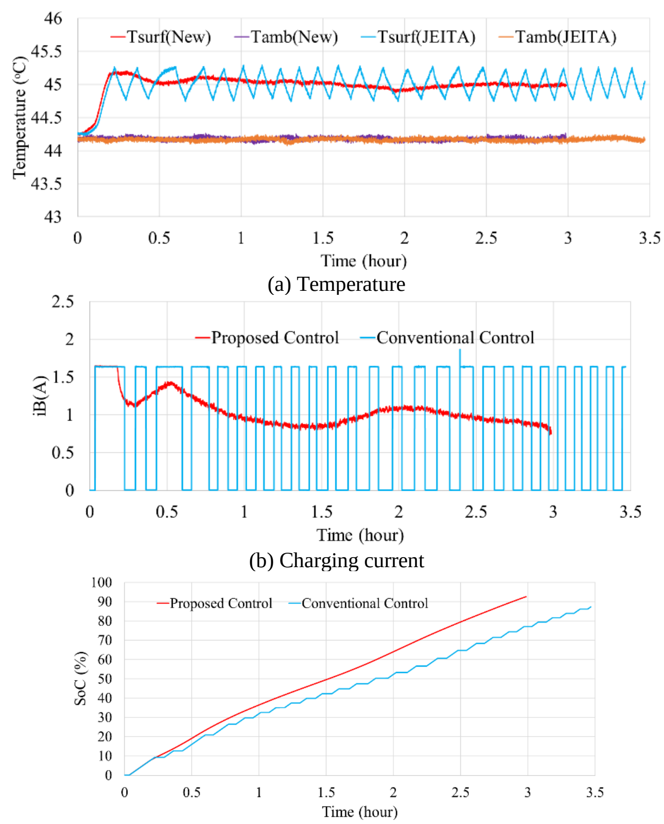

(a) Temperature

(b) Charging current

(c) SoC

Fig. 13. Measured temperatures, charging currents, and SoC of the batteries under the ambient temperature of 44.2˚C.

Experiments are also conducted under the ambient temperatures of 32.4˚C and 44.6˚C. The estimated SoC of the batteries for these two cases are plotted, as shown in Fig. 14. For T_{amb}=32.4˚C, the charging time of the conventional control is about 52.58 minutes to reach 70% SoC, while that of the proposed control is about 50.97 minutes. The charging speed is improved about 3.1%. For T_{amb}=44.6˚C, the charging time of the conventional control is about 338.46 minutes to reach 70% SoC, while that of the proposed control is only about 206.16 minutes. The charging speed can be improved about 39.09%.

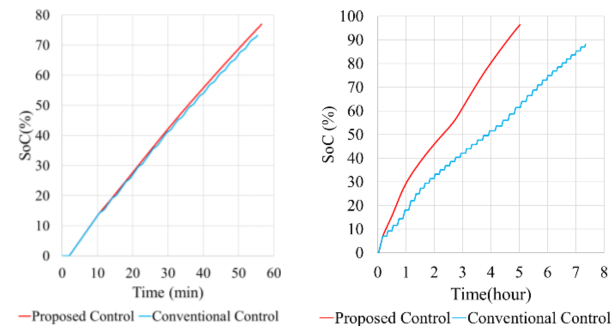

(a) (b)

Fig. 14. Estimated SoC of the batteries under (a) T_{amb}=32.4˚C and (b) T_{amb}=44.6˚C.

To indicate the charging speed improvement more explicitly, the RMS and average values of the charging currents under the four different ambient temperatures are normalized by the respective average currents of the proposed control as the variables of the y-axis in Fig. 15. Meanwhile, the average current of the proposed control is normalized by the 1C charging current (i.e., 3.35A) as the variables of the *x*-axis (i.e., X_1) in Fig. 15. The normalized average current of the conventional control is smaller than that of the proposed control (less than one) for each temperature. Besides, the differences between the normalized RMS values and average values of the proposed control are much smaller than those of the conventional control. By taking T_{amb}=44.2˚C as an example, the average charging current of the proposed control is about 0.3 C (i.e., 1A) and the corresponding RMS value is only about 1.02 times (i.e., 1.02A) of the average value. On the other hand, the average charging current of the conventional control is about 0.81 times (i.e., 0.243C, equivalent to 0.81A) that of the proposed control. The corresponding RMS value is about 1.395 times (i.e., 1.13A) of its own average value. These observations indicate that the proposed control needs less charging time than the conventional control when the heat generations are equal under different ambient temperatures. The same conclusion can also be drawn from the normalized charging time of the two control methods under the four different ambient temperatures, as shown in Fig. 16. Since the charging time of the two control methods are normalized by the charging time of the proposed control, the normalized charging time of the proposed control in Fig. 16 are all ones. Apparently, the normalized charging time of the conventional control is longer than that of the proposed control. Furthermore, the difference between RMS and average values of the conventional control become more significant when the ambient temperature increases, as shown in Fig. 15. This indicates that the charging speed improvement is more prominent when the battery is charged in a higher temperature environment. The same conclusion can also be drawn from the comparisons of the form factors between the two control methods in Fig. 16. The ratios of the form factors (i.e., form factor of the conventional control over that of the proposed control) are greater than one and this ratio increases when the ambient temperature rises. It is demonstrated that the charging speed of the proposed control improve about 25% and 66% as compared to the conventional JEITA-compliant control at T_{amb}=44.2°C and T_{amb}=44.6°C.

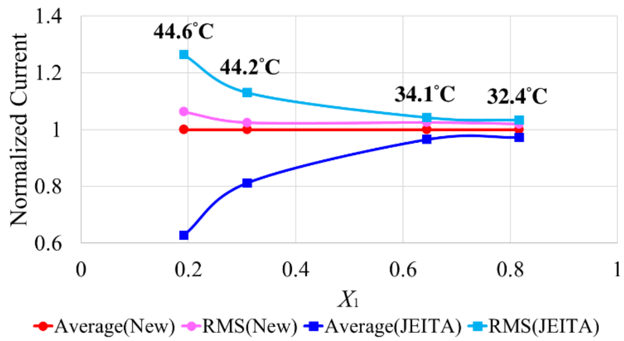

Fig. 15. Normalized RMS and average values under different ambient temperatures.

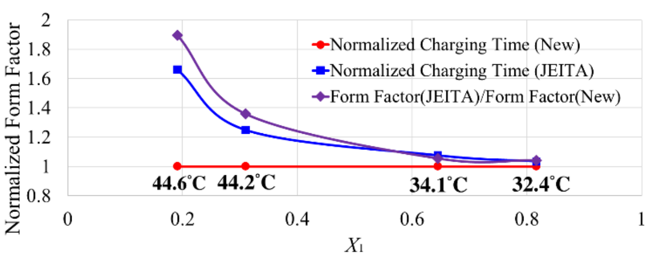

Fig. 16. Normalized charging times and form factors under different ambient temperatures.

VI. Conclusions

This paper presents a new Li-ion battery charging control strategy, namely the hybrid temperature-regulated current control (HTRCC), that can achieve higher charging speed than the existing JEITA-compliant control adopted in the industry. The proposed HTRCC is designed with the basis of the discrete temperature-regulated current control (DTRCC) of the JEITA guidelines, but it upgrades the explicit control law to a continuous control in the hysteresis band. Experimental results based on the 3350mAh Panasonic NCR18650B have confirmed that the proposed control can significantly shorten the charging time, and the improvement is more prominent for a higher ambient temperature (e.g., 66% charging speed improvement at the ambient temperature of 44.6°C). Besides, some other important conclusions can also be drawn as the supplement for the development of industrial battery charging guidelines:

1. The average battery charging current can be adopted as the key indicator for the battery charging speed. A higher average charging current can result in a faster battery charging.
2. Both the RMS and average values of a charging current can influence the dynamics of the battery temperature. The irreversible heat is determined by both values, whereas the reversible heat is only affected by the average value. Since the irreversible heat is dominant for most Li-ion batteries, the RMS value plays a significant role in the total heat generation.
3. The form factor of the charging current is an indicator for the charging speed of the control method. The charging current of a control method with a smaller form factor can lead to a faster battery charging. Because the form factor of the proposed control is one, it must be faster than the conventional control in the JEITA guidelines.

Acknowledgment

The authors would like to acknowledge the contribution of Dr. W. Wang and Dr. J. Qu for their assistances in conducting the experiment.

Appendix

A. Derivations of MCSI

Based on (15.1) and (15.2), the second partial derivatives of $\dot{Q}_{\text{total(min)}}$ and $\dot{Q}_{\text{total(max)}}$ with respect to $I_{\text{B(avg)}}$ can be derived as

$$\frac{\partial^2 \dot{Q}_{\text{total(min)}}}{\partial I_{\text{B(avg)}}^2} = 2A_1 \tag{26.1}$$

$$\frac{\partial^2 \dot{Q}_{\text{total(max)}}}{\partial I_{\text{B(avg)}}^2} = 2A_2 \tag{26.2}$$

Due to the form factor is positive, the coefficient A_2 in (15.4) must be greater than the coefficient A_1 in (15.3). Therefore, the second partial derivatives of $\dot{Q}_{\text{total(max)}}$ is greater than that of $\dot{Q}_{\text{total(min)}}$. Then, the curves of $\dot{Q}_{\text{total(min)}}$ and $\dot{Q}_{\text{total(max)}}$ versus $I_{\text{B(avg)}}$ can be plotted as shown in Fig. 17. Obviously, for the same rate of total heat generation, the average charging current $I_{\text{B(avg)(min)}}$ is greater than $I_{\text{B(avg)(max)}}$. Therefore, the MCSI can be calculated by using $I_{\text{B(avg)(min)}}$ rather than $I_{\text{B(avg)(max)}}$ as

$$MCSI = \frac{I_{\text{B(avg)}}(\text{new})}{I_{\text{B(avg)(min)}}(\text{JEITA})} \tag{27}$$

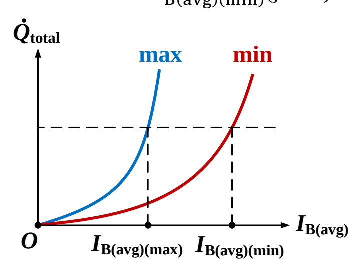

Fig. 17. Curves of $\dot{Q}_{\text{total}}$ versus $I_{\text{B(avg)}}$.

B. Proof of MCSI Being Greater Than One

Theorem 1: For 0<X<1, X<X_1<1 and 0<p<1, the *MCSI* is greater than one.

Proof:

For the investigated battery charging system, the three conditions in the **Theorem 1** are satisfied. Thus, the **Theorem 1** is validated only if

$$MCSI > 1 \tag{28}$$

By substituting (24) into (28),

$$\frac{\left[W_{(1C)}+\sqrt{W_{(1C)}^2+4pR_{B}I_{B(1C)}f_{(1C)}(X_1)}\right]X_1}{2f_{(1C)}(X_1)} > 1 \tag{29}$$

By simplifying (29) yields

$$X_1^2-(1+X)X_1+X<0 \tag{30}$$

Due to $X<X_1<1$, the equation (A5) always holds. Therefore, the **Theorem 1** is verified.

C. Determining Key Parameters for MCSI Based on Practical Measurements

The parameters p and R_B are obtained via numerous tests and fitting technique under three battery surface temperatures (i.e., 25˚C, 35˚C, and 45˚C). It is noted that the general electrical and thermal models of the battery are obtained based on multiple measurements on two different cells. The battery is charged to a designated SoC and then put to rest. The measured data and fitting curves are presented in Fig. 18 The SoC of the battery is estimated based on the CCM in (1).

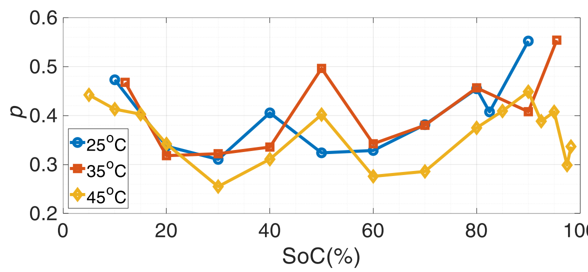

(a)

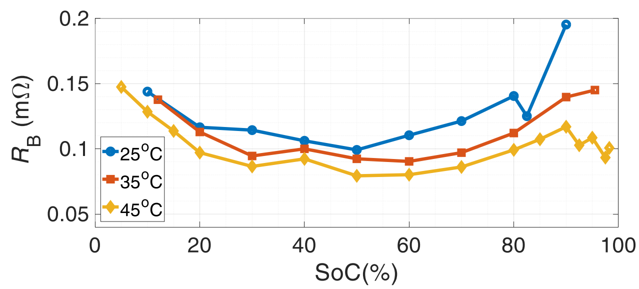

(b)

Fig. 18. Measured and fitting values of p and R_B for the NCR18650B.

Besides, the entropy coefficient $\frac{\partial V_{oc}(\mathrm{SoC})}{\partial T_{int}}$ for different SoC of the battery can be obtained by altering the temperature at a fixed SoC and then calculating the corresponding voltage change with respect to the temperature change. The curve of $\frac{\partial V_{oc}(\mathrm{SoC})}{\partial T_{int}}$ versus SoC of the battery is plotted as shown in Fig. 19.

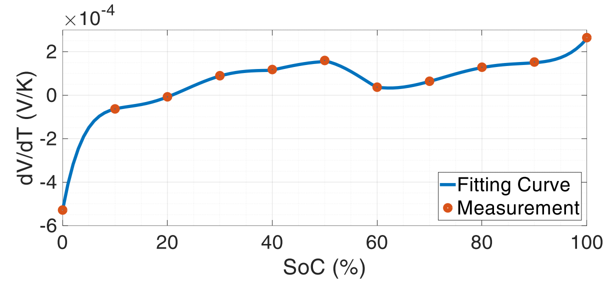

Fig. 19. The curve of the measured entropic coefficient versus SoC.

REFERENCES

[1] *[online] Battery University: BU-304a: Safety Concerns with Li-ion, 24 Sept., 2020*. Available: https://batteryuniversity.com/learn/article/safety_concerns_with_li_ion

[2] *[online] A guide to the safe use of secondary lithium ion batteries in notebook-type personal computers", Japan Electronics and Information Technology Industries Association and Battery Association of Japan, 2007*. Available: https://home.jeita.or.jp/page_file/20110517171451_cub9MvYFEh.pdf

[3] J. Qian, "Li-ion battery-charger solutions for JEITA compliance," *Texas Instruments Analog Applications Journal*, pp. 8-11, 1Q 2010.

[4] Texas Instruments, "bq5105xB High-Efficiency Qi v1.2-Compliant Wireless Power Receiver and Battery Charger," pp. 1-25, June 2017.

[5] Maxim Integrated, "MAX77301 JEITA-compliant, Li+ charger with smart power selector, automatic detectionm and USB enumeration," Sept. 2020.

[6] F. Leng, C. M. Tan, and M. Pecht, "Effect of temperature on the aging rate of Li-ion battery operating above room temperature," *Scientific Reports*, vol. 5, Aug. 2015.

[7] M. M. Kabir and D. E. Demirocak, "Degradation mechanisms in Li-ion batteries: a state-of-the-art review, " *International Journal of Energy Research*, vol. 41, no. 14, pp. 1963-1986, Nov. 2017.

[8] C. Forgez, D. V. Do, G. Friedrich, M. Morcrette, and C. Delacourt, "Thermal modeling of a cylindrical LiFePO4/graphite lithium-ion battery," *Journal of Power Sources*, vol. 195, no. 9, pp. 2961-2968, May 2010.

[9] K. Onda, T. Ohshima, M. Nakayama, K. Fukuda, and T. Araki, "Thermal behavior of small lithium-ion battery during rapid charge and discharge cycles," *Journal of Power Sources*, vol. 158, no. 1, pp. 535-542, Jul. 2006.

[10] M. Balasundaram, V. Ramar, C. Yap, L. Li, A. A. O. Tay, and P. Balaya, "Heat loss distribution: Impedance and thermal loss analyses in LiFePO4/graphite 18650 electrochemical cell," *Journal of Power Sources*, vol. 328, pp. 413-421, Oct. 2016.

[11] S. Goutam, J. M. Timmermans, N. Omar, P. Van den Bossche, and J. Van Mierlo, "Comparative study of surface temperature behavior of commercial Li-ion pouch cells of different chemistries and capacities by infrared thermography," *Energies*, vol. 8, no. 8, pp. 8175-8192, Aug. 2015.

[12] A. El Mejdoubi, A. Oukaour, H. Chaoui, H. Gualous, J. Sabor, and Y. Slamani, "State-of-charge and state-of-health Lithium-ion batteries' diagnosis according to surface temperature variation," *IEEE Trans. Ind. Electron.*, vol. 63, no. 4, pp. 2391-2402, Apr. 2016.

[13] R. Hui, *Photo-Electro-Thermal Theory for LED Systems-Basic Theory and Applicaitons*, Cambridge University Press, Sept. 2017.

[14] M. Chen and G. A. Rincon-Mora, "Accurate electrical battery model capable of predicting, runtime and I-V performance," *IEEE Trans. Energy Conver.*, vol. 21, no. 2, pp. 504-511, Jun. 2006.

[15] Z. Huang, S. C. Wong, and C. K. Tse, "Design of a single-stage inductive-power-transfer converter for efficient EV battery charging," *IEEE Trans. Veh. Technol.*, vol. 66, no. 7, pp. 5808-5821, Jul. 2017.

[16] E. X. Yang, F. C. Lee, and M. M. Jovanovic, "Small-signal modeling of series and parallel resonant converters," in *Proc. IEEE Appl. Power Electron. Conf.*, pp. 785-792, 1992.

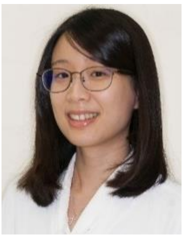

Hui-Wen Rebecca Liang received her B.S. and M.S. degrees in Electrical Engineering from National Cheng Kung University, Taiwan in 2013 and 2015, respectively. She obtained her Ph.D. degree in Electrical and Electronic Engineering from the University of Hong Kong, Hong Kong, in 2021.
From 2015 to 2017, she worked as an analog circuit engineer at Chroma ATE, Taiwan. She is currently a Teaching Fellow at the Hong Kong Polytechnic University. Her research interests include power electronics, wireless power transfer, switching power supplies, and renewable energy conversion.

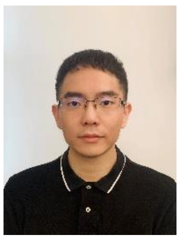

Yun Yang (M'18) received his B.Sc. degree in Electrical Engineering from Wuhan University in 2012 and Ph.D. degree in Electrical Engineering from The University of Hong Kong in 2017. He is currently a Research Assistant Professor in the Department of Electrical Engineering, the Hong Kong Polytechnic University and an Honorary Research Assistant Professor in the Department of Electrical and Electronic Engineering, the University of Hong Kong. He has authored or coauthored more than 50 technical papers, including 25 referred journal publications. He also has two book chapters and five patents and patent applications. His research interests include wireless power transfer, microgrid, power electronics and control.

S. Y. (Ron) Hui (M'87-SM'94-F'03) received his BSc (Eng) Hons in Electrical and Electronic Engineering at the University of Birmingham in 1984 and a D.I.C. and PhD in Electrical Engineering at Imperial College London in 1987. Presently, he holds the MediaTek Professorship at Nanyang Technological University and a Chair Professorship at Imperial College London. He has published over 450 research papers including 300 refereed journal publications. Over 120 of his patents have been adopted by industry. His research interests include power electronics, wireless power, sustainable lighting, and smart grid. His inventions on wireless charging platform technology underpin key dimensions of Qi, the world's first wireless power standard, with freedom of positioning and localized charging features for wireless charging of consumer electronics. He also developed the Photo-Electro-Thermal Theory for LED Systems. He received the IEEE Rudolf Chope R&D Award and the IET Achievement Medal (The Crompton Medal) in 2010 and IEEE William E. Newell Power Electronics Award in 2015. He is a Fellow of the Australian Academy of Technological Sciences & Engineering, US National Academy of Inventors and Royal Academy of Engineering, U.K.